Point-spread functions for backscattered imaging in the scanning electron microscope

Philipp Hennig, and Winfried Denk

Citation: Journal of Applied Physics **102**, 123101 (2007); doi: 10.1063/1.2817591
View online: https://doi.org/10.1063/1.2817591
View Table of Contents: http://aip.scitation.org/toc/jap/102/12
Published by the American Institute of Physics

Point-spread functions for backscattered imaging in the scanning electron microscope

Philipp Hennig[a] and Winfried Denk[b]
Max-Planck-Institute for Medical Research, Jahnstrasse 29, 69120 Heidelberg, Germany

(Received 20 May 2007; accepted 11 October 2007; published online 17 December 2007)

One knows the imaging system's properties are central to the correct interpretation of any image. In a scanning electron microscope regions of different composition generally interact in a highly nonlinear way during signal generation. Using Monte Carlo simulations we found that in resin-embedded, heavy metal-stained biological specimens staining is sufficiently dilute to allow an approximately linear treatment. We then mapped point-spread functions for backscattered-electron contrast, for primary energies of 3 and 7 keV and for different detector specifications. The point-spread functions are surprisingly well confined (both laterally and in depth) compared even to the distribution of only those scattered electrons that leave the sample again. © *2007 American Institute of Physics*. [DOI: 10.1063/1.2817591]

I. INTRODUCTION

Under certain conditions the point-spread function for optical microscopy and for transmission electron microscopes (TEM) can be derived in a straightforward manner from the physical laws governing the imaging process. The situation in the scanning electron microscope (SEM), however, where the beam hits a solid block of material, is usually dominated by multiple scattering of electrons inside the sample and closed-form solutions cannot easily, if at all, be found. Therefore, Monte Carlo simulations are usually employed to study image formation in the SEM.[1–4] Several studies have explored a number of special geometries such as thin films on top of substrates (e.g., Refs. 5 and 6), spherical inclusions at the point of beam impact,[1,7] and, more recently, objects elsewhere in the interaction volume.[8,9] These studies were applied to semiconductor samples of very heterogeneous elemental composition, for which linearity most likely does not hold. In this case any particular elemental distribution has to be subjected to a full Monte Carlo simulation (MCS). If, on the other hand, linearity can be assumed the point-spread function (PSF) completely describes the imaging process. Then and only then, the image expected for any distribution in space can be obtained by convolution.

Our study was motivated by the imaging of biological samples in the SEM using backscattering contrast.[1] This imaging modality has recently received renewed interest since it allows, in combination with an in-chamber ultramicrotome, the acquisition of stacks of sequential cross-sectional images,[10] which can then be used to reconstruct three-dimensional tissue nanostructure. For these types of imaging (serial block-face scanning electron microscopy[10]) the preparation techniques are very similar to those used in TEM of biological tissue:[11] after fixation and staining with heavy atoms (such as osmium and uranium) the tissue is dehydrated and "embedded" in a polymeric matrix (often some type of epoxy resin[12]). Such samples might be more amenable to a linear analysis of imaging properties since they essentially consist of a homogeneous background material into which a spatially inhomogeneous but dilute distribution of strong scatterers has been embedded. Even for the most densely stained material, e.g., for the widely used enzymatic precipitation of osmiophilic 3,3′-diaminobenzidine polymer,[13] the fractional concentration of heavy atoms is at most 7%, with typical values much below that.[14] In the current study we have explored the point-spread functions for this type of sample.

II. THE SIMULATION

The MCSs use as the bulk material epoxy (in our case Epon 812, which is widely used for the embedding of biological tissues[15]) and as the "point object" a small sphere, which in our case is "stained" by osmium to an atomic fraction of n_{Os}. Our simulation algorithm is based on those described in Ref. 2. To improve the accuracy we used for the calculation of path lengths between scattering events and of scattering angles numerical approximations to the partial-wave expansion approximation to the Mott cross section[16] (see Sec. V). Our algorithm also allows the simulation of samples with regions of spatially varying chemical composition.[7,17,18] Since we were interested in backscattered-electron contrast, we ignored secondary-electron generation.

The simulated path of each electron is an ordered sequence of vertices connected by straight line segments. To generate this path, a segment length is first chosen[19] from a modified Poisson distribution, which takes into account that the material composition varies along a segment if the segment intersects the test object (see Sec. V). At the end of the line segment (the "current position" at the end of the step) a chemical element (the scattering partner) is chosen stochastically from the set of elements comprising the local material. Next a scattering angle is chosen[16] at random, using the Mott cross section for the chosen element. (The azimuth is taken from a uniform distribution.) This now determines the direction of the next line segment. [The very first segment

[a]Present address: Robinson College, CB3 9AN Cambridge, United Kingdom. Electronic mail: ph347@cam.ac.uk.
[b]Electronic mail: winfried.denk@mpimf-heidelberg.mpg.de.

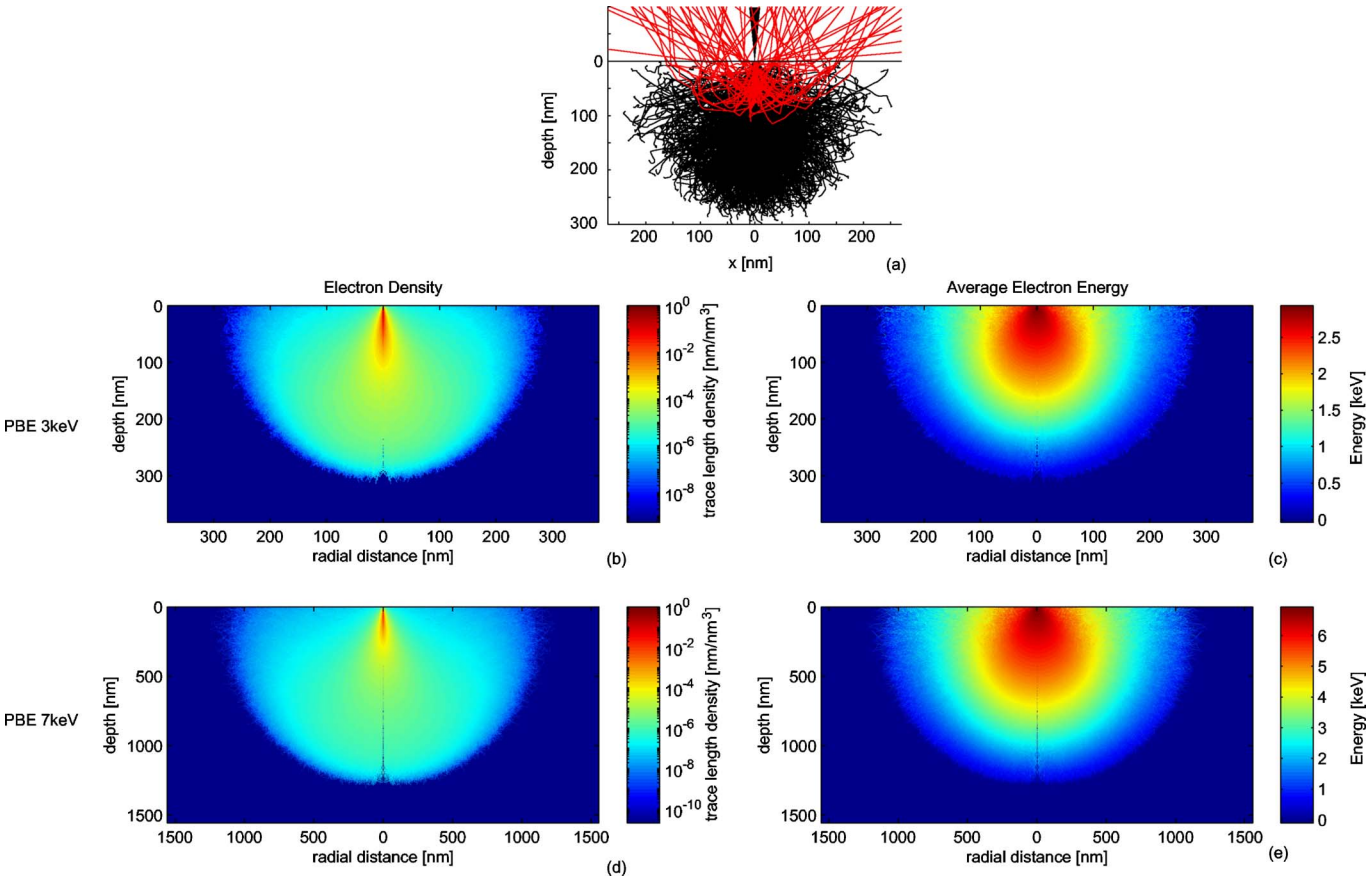

FIG. 1. (Color online) Electron trace length density and mean energy in a homogeneous sample (epoxy) around the beam impact point. 1000 simulated traces (a) of which 74 were backscattered (red) and 926 terminated in the block (black). Electron trace length densities for PBEs of 3 (b) and 7 keV (d). Mean electron energies for primary energies of 3 (c) and 7 keV (e). The singularity at the beam axis results from the way the electron density was calculated.

begins at the beam impact point (BIP) and points along the direction of the incoming beam, straight down for all results presented here]. The energy lost during a segment is calculated using the so-called continuous-slowing-down approximation,[20] which combines all inelastic electron-sample interactions. We have used Joy and Luo's[21] enhanced version of Bethe's formula[22] for the electron-energy loss. Because this approximation is only valid for energies above the average ionization energy (see Sec. V), our simulation is not suitable for the simulation of secondary electron (SE) imaging and SEs have thus been omitted.

III. RESULTS AND DISCUSSION

A. Electron trace-length density and average energy in the penetration volume

First we mapped the distribution of trace lengths and average energy (Fig. 1) around the BIP. In agreement with published work[1] we find that the penetration into the material [Figs. 1(a) and 1(c)] is strongly dependent on the primary beam energy (PBE) and that the average electron energy [Figs. 1(b) and 1(d)] decreases with lateral and vertical distance from the BIP.

B. Linearity of image formation

In order to establish that the calculation of a PSF is meaningful, we first needed to show that the process of image formation is sufficiently linear for the type of samples (epoxy-embedded biological tissue) that we are interested in. To test for linearity, we determined how well the backscattering coefficient (η) with two objects present agrees with the sum of the signals with each one of the objects present separately. For 4 nm diameter solid-osmium spheres, one of them just below the beam impact point and the other one at a variable distance into the sample, we find the behavior to be rather nonlinear for both 3 and 7 keV PBE if the spheres are close together (Fig. 2). As the osmium concentration is reduced to a plausible value (7% atomic fraction) for biological specimens the nonlinearity is much reduced (with the sum of single-sphere signals being approximately 6% and 8% larger than the two-sphere signal for 3 and 7 keV PBE, respectively) even when the spheres are touching. To examine whether cumulative effects could still affect linearity even when the osmium density was everywhere below 7%, we simulated the interaction between an Os-stained hemisphere of increasing radius, centered on the BIP, with a 4 nm sphere at a fixed depth of 12 nm below the BIP (Fig. 3). We found that the signals from sphere and hemisphere add approximately linearly over the radius range examined (Fig. 3). Even a 10 nm-radius hemisphere centered at the beam impact point reduces the signal due to the lower sphere by less than 7%. These results show that linearity is a reasonable but not a perfect assumption.

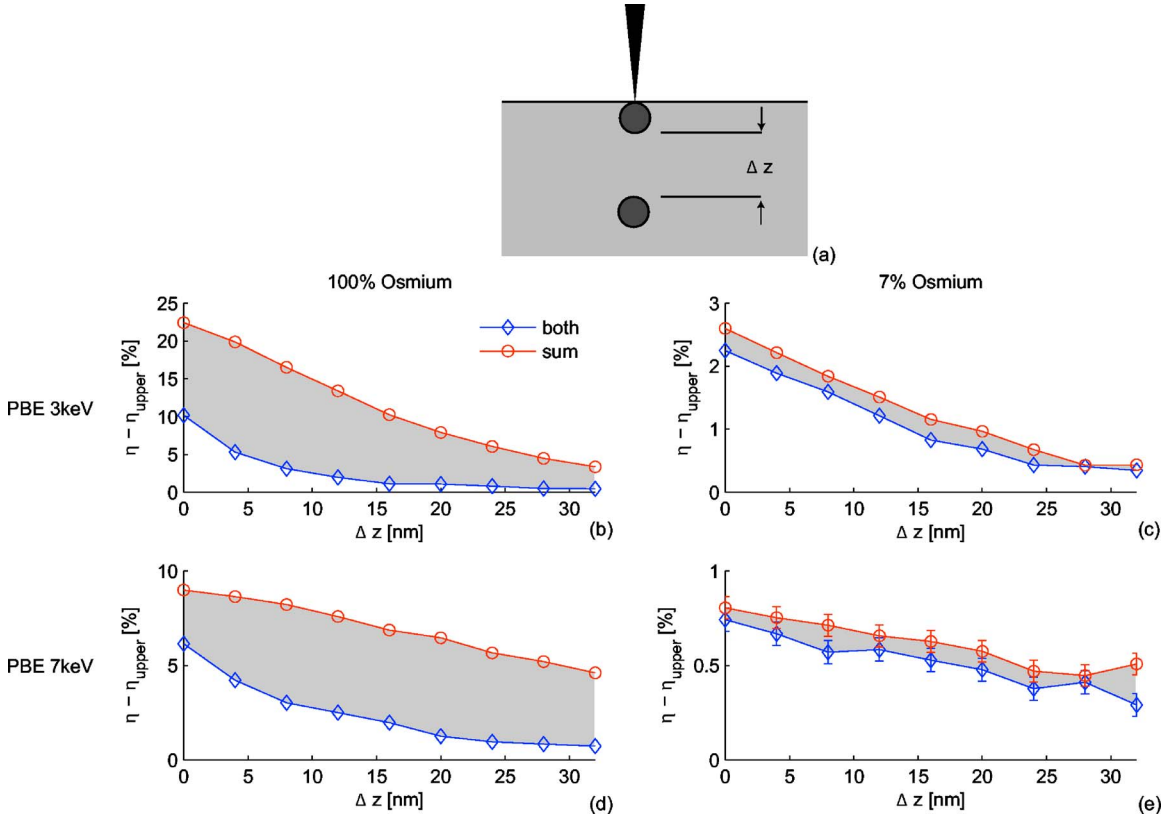

FIG. 2. (Color online) Linearity of image formation for two small objects. Simulation geometry (a) two spherical objects, one at a fixed position just below the BIP and a second, identical one at variable distance straight below. Backscattering coefficients for 100% Os [(b), (d)] and 7% Os [(c), (e)] spheres for PBEs of 3 [(b), (c)] and 7 keV [(d), (e)] as a function of the distance (Δz) between the spheres. Compared are sums (red trace) of the background-corrected backscattering coefficients ($\eta - \eta_0$) for each sphere alone with that for both spheres present (blue), where in both cases the signal of the upper sphere alone, η_{upper}, has been subtracted. The gray area between the curves indicates the nonlinearity. In (b), (c), and (d) 10^5 simulated traces were used for each data point. In (e) 10^6 traces were used per data point to achieve a satisfactory precision (note the considerable statistical fluctuation) of the signal, due to the low signal-to-noise ratio.

C. Point-spread functions

The spatial extent of the region within which an object can affect the backscattering signals depends on a number of factors. First, the scanned electron beam has a finite width at the BIP, which depends[1] on the source size, the quality of the electron optics, and on the beam current, but is, in modern SEMs with field-emission cathodes and at moderate beam currents, usually so small (even at low PBEs) that it does not affect the achievable resolution for the type of sample considered here. Second, and much more important for our sample type, is the spread of electrons in the interaction volume. In this paper we focus on this effect and, to avoid confounding the two mechanisms, assume the primary beam width to be zero. The combined effect of spot size and sample interaction can, if needed, be calculated by convolving the results of our simulations with the lateral distribution of primary electrons. To map the point spread function, we placed a test object (a sphere containing a certain concentration of Os) at a varying position around the impact point and then determined the backscattering coefficient for each position. To obtain results of sufficient precision and resolution in a reasonable time the concentration of Os and the size of the test object has to be chosen carefully. While the spatial resolution improves, of course, as the sphere gets smaller, the number of traces needed for a given accuracy increases. We found a diameter of 4 nm to be a good compromise for most of our simulations. This size is comparable to the SEM focus diameter but is still smaller than, for example, the thickness of cell membranes (5 nm). The relative density of Os (n_{Os}) was chosen such that about one scattering event by an osmium atom occurs as the electron traverses the sphere. For a 4 nm sphere a density of 12% osmium fulfills this requirement. This is slightly larger than the 7% values used for the linearity tests but we found in separate simulations (data not shown) that the signal size as a function of the Os concentration still lies in the linear range for 12% Os. We did not sample the whole interaction volume (Fig. 1) for the full simulations because preliminary results made it clear that the test object had a discernable effect on the backscattering coefficient only in a small fraction of the penetration volume.

The PSFs (Fig. 4) for PBEs of both 3 [Fig. 4(b)] and 7 keV [Fig. 4(c)] become indistinguishable from the background noise [i.e., the statistical fluctuation of the simulated epoxy backscattered electron (BS4) signal] at depths much smaller than the penetration of electrons into the sample (Fig. 1). While the actual PSF is expected to start increasing in width immediately below the surface, the finite size of the test sphere dominates the width of our simulated PSF close to the sample surface [Fig. 4(d)]. Only deeper in the sample

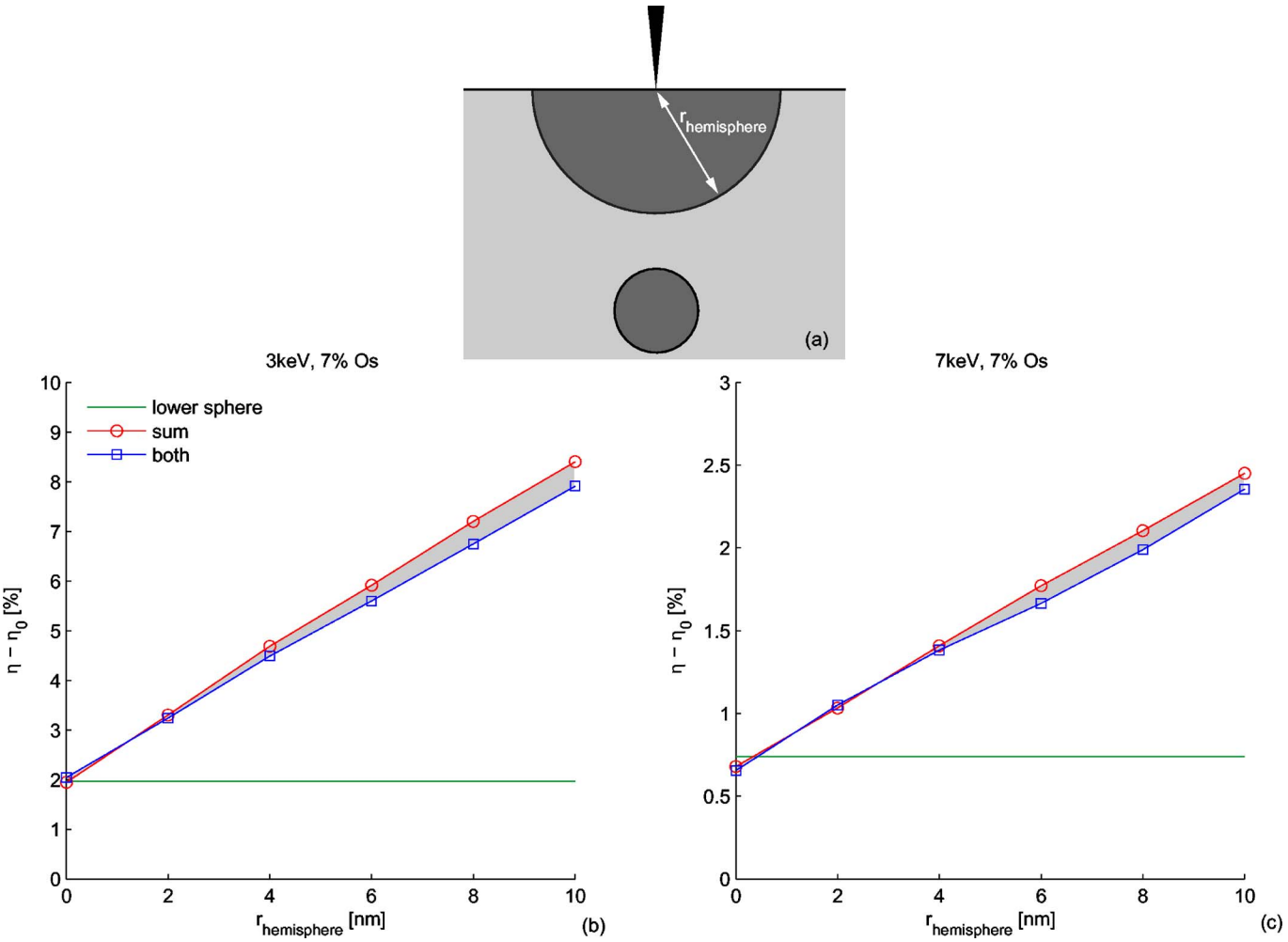

FIG. 3. (Color online) Linearity of image formation for one large and one small object. The simulation geometry (a) comprises a hemispherical object of variable radius centered on the BIP and a 7% Os spherical object of 4 nm diameter at a depth of 12 nm. Background-corrected backscattering coefficient ($\eta - \eta_0$) as a function of the hemisphere radius for PBEs of 3 (b) and 7 keV (c). Plotted are the signals of the fixed sphere (green), the growing hemisphere alone (red), which is shifted upwards by the signal of the deep sphere alone, and the signal with both spheres present (blue). The gray area between the red and the blue lines indicates the nonlinearity. Each data point represents 10^6 simulated traces.

does the increasing lateral width of the PSF due to spreading of the electrons from the beam axis become apparent [Fig. 4(e)].

The signal-to-noise ratio falls off with rising primary beam energy (from $\eta_{max}/\eta_0 \approx 1.8$ for 3 keV to $\eta_{max}/\eta_0 \approx 1.2$ for 7 keV for our particular choice of sphere size and osmium concentration, where η_{max} denotes the backscattering coefficient for a sphere position directly underneath the BIP and η_0 denotes the backscattering coefficient of epoxy with no stained sphere present).

We next explored how energy and angular distributions of BS electrons depend on the presence of the heavy metal-stained sphere (Fig. 5). Without the test sphere the energy distribution follows the broad distribution typical for backscattering from light elements[23–25] and the angular distribution is almost perfectly Lambertian, as expected for diffusing electrons.[1,26] With the sphere placed directly underneath the BIP a strong peak appears in the energy spectrum just below the primary energy [Fig. 5(a)] and the angular distribution [Fig. 5(b)] deviates from a Lambertian behavior, with more electrons emerging at smaller angles from the surface normal, which has also been observed experimentally.[27,28] The angular distribution of BSEs with an energy loss of less than 300 eV closely resembles the backward portion of the Mott cross section used to generate Os scattering angles [Fig. 5(b)]. Those observations are consistent with the fact that heavy atoms (Os in this case) have larger average scattering angles and thus cause many more scattering events with large scattering angles, which contribute very efficiently to the generation of backscattered electrons. If the trajectory direction is turned around with few, maybe even a single, scattering event(s) the path length inside the sample is small, and so is the energy loss. We found it to be crucial to use the full Mott distribution for osmium, rather than the approximation based on transport cross sections[16,29,30] used for the remaining bulk elements (see Sec. V), which is appropriate only when many scattering events occur, but will lead to spurious BSEs at high angles (data not shown), when used for osmium in our scattering geometry.

Given that energy and angular distributions are changed substantially by the presence of heavy-atom objects, we next explored how selecting the backscattered electrons according to energy and angle affects the PSF (Fig. 6). If we simply use the angular acceptance range and the energy-dependence of a

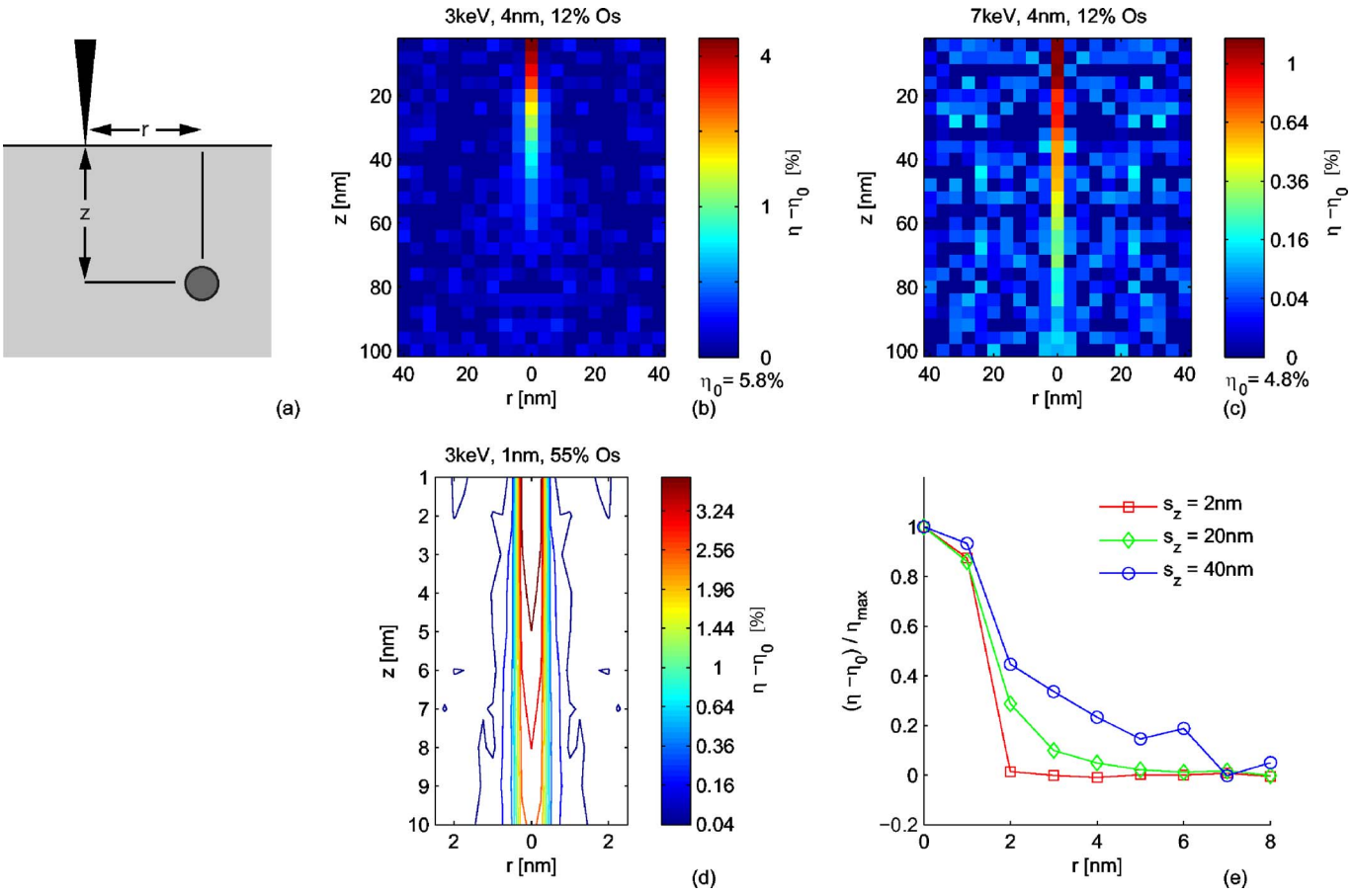

FIG. 4. (Color online) Point-spread functions. Principle of PSF mapping (a) an Os containing sphere [12% Os and 4 nm diameter for panels(b), (c), and (e)] is placed at different depths, z, and radial distances, r, from the BIP. The PSFs for PBEs of 3 (b) and 7 keV (c). The region (d) close to the beam impact point was sampled again at higher resolution, using a smaller sphere (1 nm diameter, 55% Os). Each simulation contains $\approx 10^6$ traces. The spacing in the color scale is roughly proportional to the square root of the signal. η_0 is 5.82% for 3 and 4 keV, 4.76% for 7 keV. Horizontal (e) cross sections through the PSF at different depths, normalized to their peaks, sampled at a higher lateral resolution, using 10^6 traces per data point. Note that absolute values are displayed (due to noise $\eta - \eta_0$ can go slightly negative).

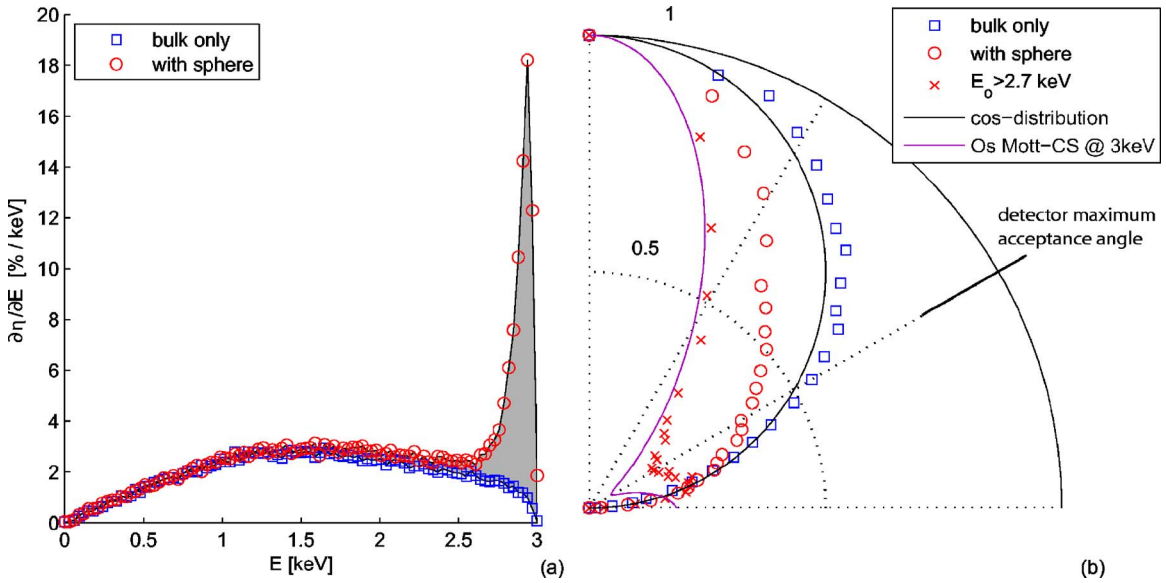

FIG. 5. (Color online) Energy (a) and angular (b) distributions for BSEs with and without a 4 nm, 7% Os sphere directly underneath the BIP. Angular distributions (b) of all BSEs with (red circles) and without (blue squares) the Os sphere. Also shown (red crosses) are the distribution of electrons with $E_i > 2.7$ keV, a Lambertian (cosine) distribution (black line), and the differential elastic Mott cross section for backward scattering (violet line). Each MCS contains 10^6 electron traces with a PBE of 3 keV. Even though the total number of BSEs is larger (by 46%) with the Os sphere, the angular histograms in (b) were normalized to their values at the surface normal to facilitate comparison.

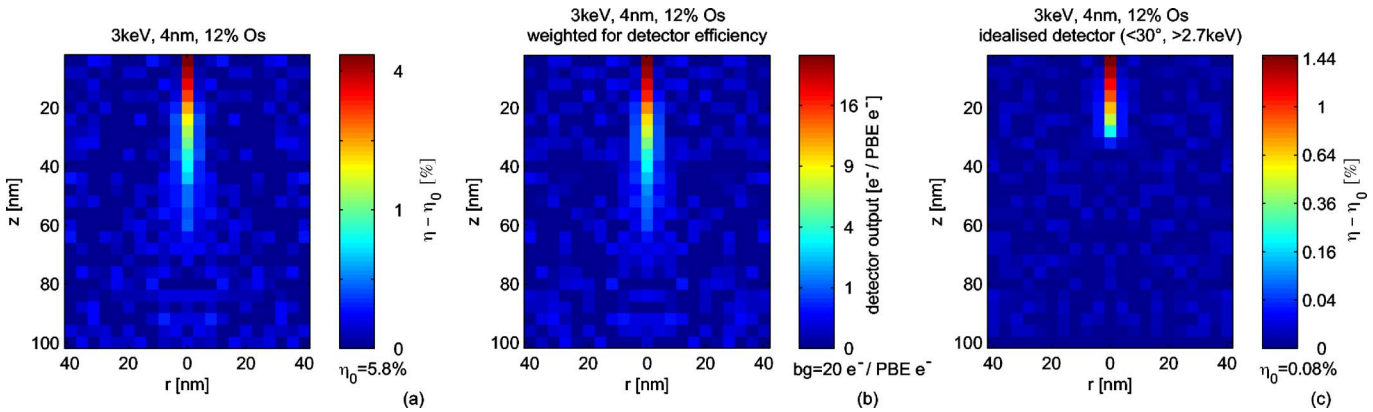

FIG. 6. (Color online) Effect of the detector energy and angle sensitivity on the PSF. The PSF when counting [(a), which is identical to Fig. 4(b)] all electrons that emerge with equal weight, irrespective of angle and energy, does not change much when taking into account (b) the typical acceptance angle (60° from the surface normal) and the energy sensitivity of a silicon-diode detector [given in (b) are the number of electrons generated in the diode per incident electron]. A hypothetical detector (c) selecting only electrons within a 30° angle from the surface normal and sharply cutting off electrons with energies below 2.7 keV (for a PBE of 3 keV) shows a PSF penetrating considerably less deep into the sample and also shows a higher signal to noise ratio.

realistic detector, such as a PIN silicon detector diode, where the charge generated is roughly proportional to the electron energy (IRD AXUV), see Ref. 31, we find the PSF to be nearly unaffected [Fig. 6(b)]. But if we used a hypothetical detector that has a much narrower angular acceptance (30 degrees from the axis) and detects only electrons that have lost less than 10% of their energy the PSF extends much less deep into the sample [Fig. 6(c)], while at the same time the signal-to-noise ratio appears to be improved.

When we explore the falloff of the PSF with depth in more detail (Fig. 7) we find a somewhat complicated picture and that the use of a single information depth[1] is misleading. Along the beam axis the falloff is rather fast, much faster even than the distribution of backscattered electrons. Next to the beam axis the maximal intensity is reached deeper inside the sample and the decay with depth is much slower. If we test how a heavy-atom stained horizontal plane affects the backscattering coefficient we find that such a plane has a strong effect on backscattering, even when it is located beyond the depth to which backscattered electrons normally reach, indicating that such a plane changes the directional distribution of electrons deeper in the sample such that otherwise-absorbed electrons are converted into backscattered electrons. This situation somewhat resembles that of wide-field fluorescence microscopy, where the resolution along the optical axis is poor for low spatial frequencies, i.e.,

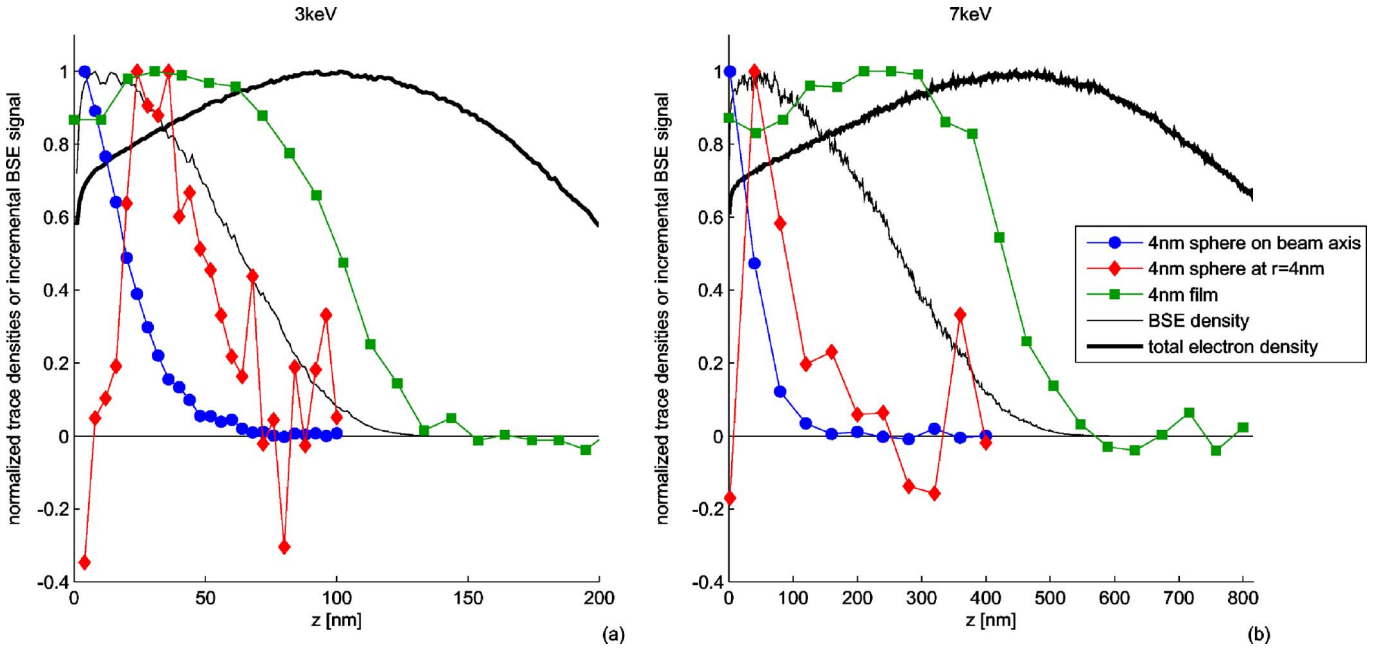

FIG. 7. (Color online) Falloff with depth of the electron trace density counting all electrons (thick black lines), the density of those electrons (backscattered electrons, thin black line) that leave the sample again, and the backscattering coefficient for a 4 nm, 12% Os sphere on the beam axis (blue disks) and at 4 nm radial distance (red diamonds), and a 4 nm thick film (green squares) of stained material (12% Os). All falloffs are plotted at PBEs of 3 (a) and 7 keV (b). The red and blue lines in (a) represent 10^6 traces, the green line 10^4 traces. In (c), the red and blue lines represent approximately 10^7 traces, the green line represents roughly 10^6 traces. All data sets were normalized to a maximal value of 1. The ratio of the depth scales is $(3/7)^{1.67}$, following a commonly used model for the scaling of penetration depths (Ref. 32).

large objects, but small structures can be resolved quite well. Our PSF data suggest that for samples such as brain tissue, where most important structural detail is on a small spatial scale, the effective z resolution is much better than the depth to which backscattered electrons penetrate, which is somewhat similar to the situation in the transmitted-light microscopy, where although light penetrates the whole sample the z location of small structures can be quite well determined.

IV. CONCLUSION

We have shown that for the concentrations of heavy atoms typical for biological tissue embedded in a polymer matrix backscattered-electron image formation is sufficiently linear to justify the use of superposition. Our most surprising result is the steep falloff of the PSF with depth, which is much steeper than the density of electron trajectories that eventually emerge from the sample. Thus estimates of the information depth in SEM imaging,[1] which used this density need to be used cautiously.

V. METHODS

The unstained parts of the sample are assumed to consist of epoxy with an elemental composition (mostly hydrogen, carbon, and oxygen) of the widely used Epon 812 resin. Its mass density is $\rho_{\mathrm{Ep}}=1.22\ \mathrm{g/cm^3}$ and the atomic (molar) fractions are $n_{\mathrm{H}}=0.53$, $n_{\mathrm{C}}=0.35$, $n_{\mathrm{O}}=0.12$, (according to data sheets provided by a supplier, Serva Electrophoresis GmbH, Heidelberg, Germany). The atom density is then $N=\rho_{\mathrm{Ep}}N_{\mathrm{Av}}\Sigma_{i\in\{\mathrm{H,C,O}\}}n_i/A_i$ (where N_{Av} is Avogadro's constant and the $A_i s$ are the atomic masses). In the stained regions, the atomic fractions are $n_i'=(1-n_{\mathrm{Os}})n_i$ and the number density is $N'=\rho' N_{\mathrm{Av}}\Sigma_{i\in\{\mathrm{H,C,O,Os}\}}n_i/A_i$ with $\rho'=(1-n_{\mathrm{Os}})\rho_{\mathrm{Ep}}+n_{\mathrm{Os}}\rho_{\mathrm{Os}}$, where $\rho_{\mathrm{Os}}=22.61\ \mathrm{g/cm^3}$ is the density of pure Os.

The calculation of a trajectory proceeds as follows. The electron starts at a particular location in a defined direction. At the very beginning the location is the beam impact point, the direction is along the beam axis (i.e., straight down), and the energy is the PBE. First, the distance to the next scattering event is determined stochastically using a probability distribution given by $d[p(x)]/dx$, where $p(x)$ is the probability that the electron has not yet been scattered and x is the distance along the segment. At the start of a segment ($x=0$) we have $p(x=0)=1$ and we know that

$$dp(x)/dx = p(x)/\lambda(x) = p(x)N\sigma_T(x) = p(x)N\sum_i n_i\sigma_i,$$

where $\lambda(x)$ is the mean free path, $\sigma_T(x)$ is the total cross section, and the $\sigma_i' s$ are the single-element elastic scattering cross sections.[33] If the material composition is homogeneous $p(x)=\exp(-x/\lambda)$. If the path crosses the test object there will be a region of different composition between, say, x_1 and x_2, then

$$p(x)=\begin{cases}\exp\left(-\dfrac{x}{\lambda_b}\right) & \text{for } 0<x<x_1\\ \exp\left(-\dfrac{x_1}{\lambda_b}+\dfrac{x_1}{\lambda_h}\right)\exp\left(-\dfrac{x}{\lambda_h}\right) & \text{for } x_1<x<x_2\\ \exp\left(-\dfrac{x_1-x_2}{\lambda_b}-\dfrac{x_2-x_1}{\lambda_h}\right)\exp\left(-\dfrac{x}{\lambda_b}\right) & \text{for } x_2<x\end{cases},$$

where λ_b and λ_h are the mean free paths in the bulk and in the stained region, respectively.

Using a uniformly distributed random variable $R\in[0,1]$ we can draw a free path

$$x(R)=\begin{cases}x_0-\lambda_b\ln(R) & \text{if } R<\exp(-x_1/\lambda_b)\\ x_0-\lambda_h[(\lambda_b^{-1}-\lambda_h^{-1})(x_1-x_0)+\ln(R)] & \text{if } \exp(-x_1/\lambda_b)<R<\exp[-(x_1-x_2)/\lambda_h-x_1/\lambda_b]\\ x_0-\lambda_b[(\lambda_h^{-1}-\lambda_b^{-1})(x_2-x_1)+\ln(R)] & \text{if else}\end{cases}.$$

To determine the flight direction for the next segment, we choose an element stochastically[18] using the elemental composition at the end of the current segment, each element having the probability $P_i=n_i\sigma_i/\sigma_T$, (where $i\in\{\mathrm{H,C,O,Os}\}$), then draw a scattering angle. For osmium, which has a differential scattering cross section of considerable complexity, tables of precalculated values for the partial-wave expansion approximation to the differential elastic Mott scattering cross section were used.[34] The type of binning used in Ref. 34 proved, however, too coarse for the simulation of bulk elements, especially at PBEs above 5 keV. For these elements, the following approximation to the differential Mott cross section was used[16,30] instead:

$$\frac{d\sigma}{d\Omega}=\frac{\sigma_{\mathrm{el}}}{4\pi}\frac{Y(Y+2)}{(1-\cos\theta+Y)^2},$$

where σ_{el} is the total Mott scattering cross section (taken from precalculated values using the partial wave expansion approximation[29]), θ is the scattering angle, and Y is a parameter found by imposing

$$\int (1-\cos\theta)\frac{d\sigma}{d\Omega}d\Omega \stackrel{!}{=} \sigma_{\mathrm{tr}},$$

where σ_{tr} is the transport cross section, which was also tabulated in Ref. 29. This approximation ensures, by construction, that average scattering angles are conserved and is at energies used here a good approximation for the light elements, since deviations from the full partial wave expansion are averaged out due to the large number of consecutive scattering events.[35] Using only the elastic scattering cross section leads to a systematic underestimation of the segment lengths. This error is, however, small ($\sim 1\%-2\%$ relative change in signal[36]) and we have neglected it.

For PSF mapping, we chose the Os concentration, n_{Os}, such that for an electron traversing the test sphere the average number of scattering events ($P_{\mathrm{Os}} 2r/\lambda_h$, with r the sphere radius, P_{Os} defined analogous to P_i earlier.) involving osmium as the scattering partner is about 1.

The energy loss along the segment length Δs is determined by using the stopping-power formula by Joy and Luo[2,21] (which incorporates low energy corrections to Bethe's[22] original formula)

$$\frac{dE}{ds} = -78\,500\frac{N}{N_{\mathrm{Av}}}\frac{1}{\sum_i n_i/A_i}\frac{\bar{Z}}{\bar{A}E}\ln\left[\frac{1.166(E+0.85\bar{J})}{\bar{J}}\right],$$

where ρ is the local mass density, while $\bar{Z}$, $\bar{A}$, and $\bar{J}$ are the weighted averages of nuclear charge, nuclear mass, and mean ionization energy, respectively, using the $P_i s$ as weights. If a segment intersects regions that differ in elemental composition the energy loss is calculated for each region separately.

Each electron trajectory is followed until either the electron energy falls below the mean ionization energy[2,32] of the heaviest bulk element, $J_{\mathrm{O}}=(9.76+58.8\cdot Z^{-0.19})$ eV, which is ≈ 110 eV for oxygen, or the electron leaves the sample. (Osmium stained areas were only simulated in sample regions with average electron energies far above J_{Os}.) The whole simulation was written in MATLAB and is capable of generating electron traces at a frequency of about 200–300 Hz on standard contemporary computer hardware (3 GHz Intel Pentium 4, 2 GB RAM).

For the calculation of radial electron trace-length densities (Fig. 1), individual trace segments are broken up into subsegments of 0.1 nm length and individually placed in radial/depth bins (1 nm wide in the radial and depth directions). The trace density was corrected for the fact that the bin volume is proportional to $2\pi r$. This, however, causes an artifact for $r=0$ (visible in Fig. 1). Horizontal integrals of electron trace densities at depth z (black curves in Fig. 5) were calculated as the sum of subsegments intersecting a horizontal plane at depth z, weighted by $1/\cos(\vartheta)$, where ϑ is the angle between the segment and the horizontal plane.

[1] J. I. Goldstein, D. E. Newbury, D. C. Joy, C. Lyman, P. Echlin, E. Lifshin, L. Sawyer, and J. Michael, in *Scanning Electron Microscopy and X-Ray Microanalysis*, 3rd ed. (Plenum, New York, 1992).
[2] D. C. Joy, *Monte Carlo Modeling for Electron Microscopy and Microanalysis* (Oxford University Press, New York, 1995).
[3] H. E. Bishop, Thesis, University of Cambridge, 1966.
[4] R. Shimizu, K. Murata, and G. Shinoda, in *X-Ray Optics and Microanalysis*, edited by R. Castaing, P. Descamps, and J. Philbert, 1965), p. 127.
[5] M. Dapor, Phys. Rev. B **46**, 618 (1992).
[6] K. L. Hunter, I. K. Snook, and H. K. Wagenfeld, Phys. Rev. B **54**, 4507 (1996).
[7] R. Gauvin, P. Hovington, and D. Drouin, Scanning **17**, 202 (1995).
[8] Z. J. Ding and H. M. Li, Surf. Interface Anal. **37**, 912 (2005).
[9] Y. T. Yue, H. M. Li, and Z. J. Ding, J. Phys. D **38**, 1966 (2005).
[10] W. Denk and H. Horstmann, PLoS Biol. **2**, e329 (2004).
[11] G. E. Palade, J. Exp. Med. **95**, 285 (1952).
[12] M. A. N. Hajibagheri, *Electron Microscopy Methods and Protocols* (Humana, Totowa, NJ, 1999).
[13] R. C. Graham and M. J. Karnovsky, J. Histochem. Cytochem. **14**, 291 (1966).
[14] J. S. Hanker, W. A. Anderson, and F. E. Bloom, Science **175**, 991 (1972).
[15] H. Finck, J. Biophys. Biochem. Cytol. **7**, 27 (1960).
[16] M. Dapor, *Electron-Beam Interactions with Solids: Application of the Monte Carlo Method to Electron Scattering Problems* (Springer, Berlin, 2003).
[17] R. Gauvin, G. Lesperance, and S. Stlaurent, Scanning **14**, 37 (1992).
[18] P. G. T. Howell and A. Boyde, Scanning **20**, 45 (1998).
[19] K. Murata, H. Kawata, K. Nagami, Y. Hirai, and Y. Mano, J. Vac. Sci. Technol. B **5**, 124 (1987).
[20] L. V. Spencer and U. Fano, Phys. Rev. **93**, 1172 (1954).
[21] D. C. Joy and S. Luo, Scanning **11**, 176 (1989).
[22] H. Bethe, Ann. Phys. **397**, 325 (1930).
[23] W. Bothe, Z. Naturforsch. A **4A**, 542 (1949).
[24] W. Bothe, Ann. Phys. **6**, 44 (1949).
[25] D. E. Newbury and R. L. Myklebust, in "Microbeam Analysis," edited by D. G. Howitt (San Francisco Press, San Francisco, 1991), pp. 561–564.
[26] W. Bothe, Z. Phys. **54**, 161 (1929).
[27] W. Oppel and H. Jahrreis, Z. Phys. **252**, 107 (1972).
[28] F. Tesar and L. Eckertov, Czech. J. Phys., Sect. B **23**, 867 (1973).
[29] R. Mayol and F. Salvat, At. Data Nucl. Data Tables **65**, 55 (1997).
[30] J. Baro, J. Sempau, J. M. Fernandezvarea, and F. Salvat, Nucl. Instrum. Methods Phys. Res. B **84**, 465 (1994).
[31] Detector Quantum Efficiency data sheet provided by manufacturer at http://www.ird-inc.com/text/axuvopeprin.txt.
[32] K. Kanaya and S. Okayama, J. Phys. D **5**, 43 (1972).
[33] R. Herrmann and L. Reimer, Scanning **6**, 20 (1984).
[34] A. Jablonski and S. Tougaard, Surf. Interface Anal. **22**, 129 (1994).
[35] R. Browning, T. Z. Li, B. Chui, J. Ye, R. F. W. Pease, Z. Czyzewski, and D. C. Joy, J. Appl. Phys. **76**, 2016 (1994).
[36] A. Jablonski, C. J. Powell, and S. Tanuma, Surf. Interface Anal. **37**, 861 (2005).